

## Three-Mode Variable-Frequency Modulation for the Four-Switch Buck-Boost Converter A QR-BCM Versus TCM Case Study and Implementation

Vermeer, Wiljan; Wolleswinkel, Marck; Schijffelen, Jos; Chandra Mouli, Gautham Ram; Bauer, Pavol

**DOI**

[10.1109/TIE.2024.3390734](https://doi.org/10.1109/TIE.2024.3390734)

**Publication date**

2025

**Document Version**

Final published version

**Published in**

IEEE Transactions on Industrial Electronics

**Citation (APA)**

Vermeer, W., Wolleswinkel, M., Schijffelen, J., Chandra Mouli, G. R., & Bauer, P. (2025). Three-Mode Variable-Frequency Modulation for the Four-Switch Buck-Boost Converter: A QR-BCM Versus TCM Case Study and Implementation. *IEEE Transactions on Industrial Electronics*, 72(2), 1512-1523. <https://doi.org/10.1109/TIE.2024.3390734>

**Important note**

To cite this publication, please use the final published version (if applicable).  
Please check the document version above.

**Copyright**

Other than for strictly personal use, it is not permitted to download, forward or distribute the text or part of it, without the consent of the author(s) and/or copyright holder(s), unless the work is under an open content license such as Creative Commons.

**Takedown policy**

Please contact us and provide details if you believe this document breaches copyrights.  
We will remove access to the work immediately and investigate your claim.





***Green Open Access added to TU Delft Institutional Repository***

***'You share, we take care!' - Taverne project***

**<https://www.openaccess.nl/en/you-share-we-take-care>**

Otherwise as indicated in the copyright section: the publisher is the copyright holder of this work and the author uses the Dutch legislation to make this work public.

# Three-Mode Variable-Frequency Modulation for the Four-Switch Buck-Boost Converter: A QR-BCM Versus TCM Case Study and Implementation

Wiljan Vermeer , Member, IEEE, Marck Wolleswinkel , Jos Schijffelen ,  
Gautham Ram Chandra Mouli , Member, IEEE, and Pavol Bauer , Senior Member, IEEE

**Abstract**—Quasi-resonant boundary-conduction mode (QR-BCM) and triangular current mode (TCM) have found widespread use in the literature and industry due to their good performance at relatively low complexity. However, additional control challenges occur when these modulations are applied to the four-switch buck-boost (FSBB) converter, due to a discontinuity in switching frequency in multimode operation. This article presents the first closed-loop operation of a variable-frequency, multimode, quasi-resonant BCM control scheme including smooth mode transitions. The proposed control utilizes feed-forward mode transition techniques, based on software interrupt handlers integrated into the digital control scheme. In contrast to most soft-switching schemes in the literature, the proposed digital control does not imperatively rely on high-frequency current measurements but uses dc measurements and high-frequency voltage measurements instead. A 10 kW prototype is developed with which the proposed modulation is compared with three other soft-switching modulation schemes. Our results indicate that the losses of FSBB converter can be reduced by up to 60% using the proposed modulation. Especially at partial powers and high voltages, significant efficiency gains can be achieved.

**Index Terms**—Cascaded buck-boost, closed-loop control, dc–dc converter, mode transitions, soft switching.

## I. INTRODUCTION

**B**ECAUSE of its bidirectional buck and boost capabilities and relatively low-component stress, the four-switch buck-boost (FSBB) converter is a common topology for applications with overlapping in- and output voltages, such as battery

Manuscript received 29 August 2023; revised 27 December 2023 and 10 March 2024; accepted 5 April 2024. Date of publication 26 July 2024; date of current version 24 December 2024. This work was supported by TKI Urban energy. (Corresponding author: Wiljan Vermeer.)

Wiljan Vermeer, Gautham Ram Chandra Mouli, and Pavol Bauer are with the TU Delft, 2628CD Delft, The Netherlands (e-mail: w.w.m.vermeer@tudelft.nl; g.r.chandramouli@tudelft.nl; p.bauer@tudelft.nl).

Marck Wolleswinkel is with the Reconvert BV, 3439MP Nieuwegein, The Netherlands (e-mail: marck.wolleswinkel@reconvert.eu).

Jos Schijffelen is with the Power Research Electronics BV, 4817ZK Breda, The Netherlands (e-mail: jos.schijffelen@heliox-energy.com).

Digital Object Identifier 10.1109/TIE.2024.3390734

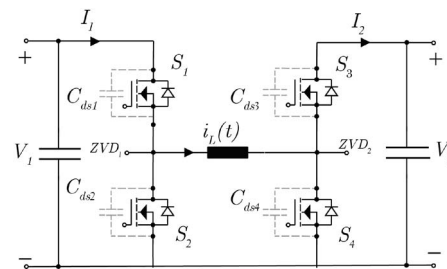


Fig. 1. Cascaded buck-boost converter topology.

systems, electrolyzers, PV systems, and electric vehicles [1], [2], [3]. Fig. 1 shows the FSBB topology. This study focuses on the design and comparison of a soft-switching modulation scheme for the FSBB converter, designed to be able to operate in a wide-voltage and power range, to make it suitable for a wide range of PV and battery applications.

The four switches of the FSBB converter result in a high degree of freedom in terms of pulse width modulation (PWM). Due to this high degree of freedom, and its widespread applicability, the different modulation schemes for the FSBB converter have been significantly investigated. Table I summarizes the related studies regarding soft-switching modulation strategies for the FSBB. The comparison criteria includes the number of control variables ( $N_{ctrl}$ ), whether it includes interleaving (Interl.), the controller used (Control), maximum power (Power), and peak efficiency ( $\eta_{pk}$ ).

The studies can be divided into two parts.

- 1) Constant-frequency (CF) modulation, such as quadrilateral current modulation (QCM).
- 2) Variable-frequency (VF) modulation techniques, for example, triangular current modulation (TCM) or boundary-conduction mode (BCM) [or quasi-resonant BCM (QR-BCM)].

The basic switching waveforms of these modulations are shown in Fig. 2. The QCM modulation strategies operate at a constant frequency and modulate the current such that ZVS turn-on is possible for every switch. The high degree of freedom (the duty cycle of each half-bridge  $D_{S1}$ ,  $D_{S3}$  and the phase-shift  $\theta$  between them) can be used for various objectives such as to:

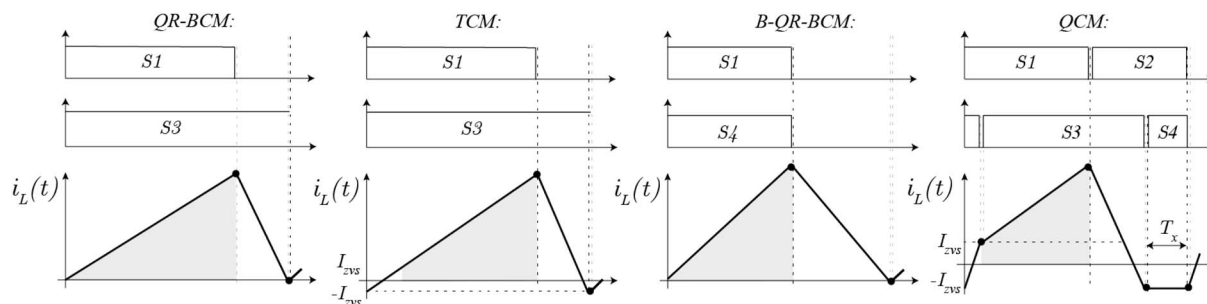


Fig. 2. Gate signals and inductor current for QR-BCM, TCM, bipolar QR-BCM (B-QR-BCM), and QCM [4]. The grey area under the current waveform represents the amount of power transferred. For simplicity, all switching instances are depicted as ideal. However, all strategies employ quasi-resonant switching to achieve ZVS or ZCS. Please note that the QR-BCM, TCM, and QCM modulation schemes are depicted in buck mode. The switching waveforms can vary depending on the in- and output voltage ratio.

TABLE I  
RELATED STUDIES REGARDING SOFT-SWITCHING MODULATION STRATEGIES FOR THE FSBB

Study	Modulation	ZVS	$N_{ctrl}$	Interl.	Control	Power	$\eta_{pk}$
[1]	CF-QCM	✓	3	x	PI	300 W	98.5%
[2]	CF-QCM	✓	3	x	x	3 kW	99.4%
[3]	CF-QCM	✓	3	x	LUT	300 W	98%
[4]	QCM+QR-BCM	ZVS/ZCS	1	x	x	3 kW	98.1%
[5]	CF-QCM	✓	3	✓	LUT	12 kW	98.3%
[6]	CF-QCM	✓	3	x	x	200 W	97.8%
[7]	CF-QCM	✓	2	x	LUT	200 W	98.8%
[8]	CF-QCM	✓	3	x	Type-I	500 W	98.7%
[9]	CF-QCM	✓	3	x	LUT	280 W	98.1%
[10]	CF-QCM	✓	2	x	LUT	1.5 kW	99%
[11]	CF-QCM	✓	2	x	LUT	250 W	98%
[12]	VF-QCM	✓	3	x	x	3 kW	99.6%
[13]	TCM+B-QR-TCM	✓	1	x	x	1 kW	99.5%
[14]	QR-BCM	✓	1	x	x	500 W	97%
[15]	TCM	✓	1	x	PI	3 kW	99.6%
Prop.	QR-BCM	ZVS/ZCS	1	✓	Type-III & FF	10 kW	99.6%

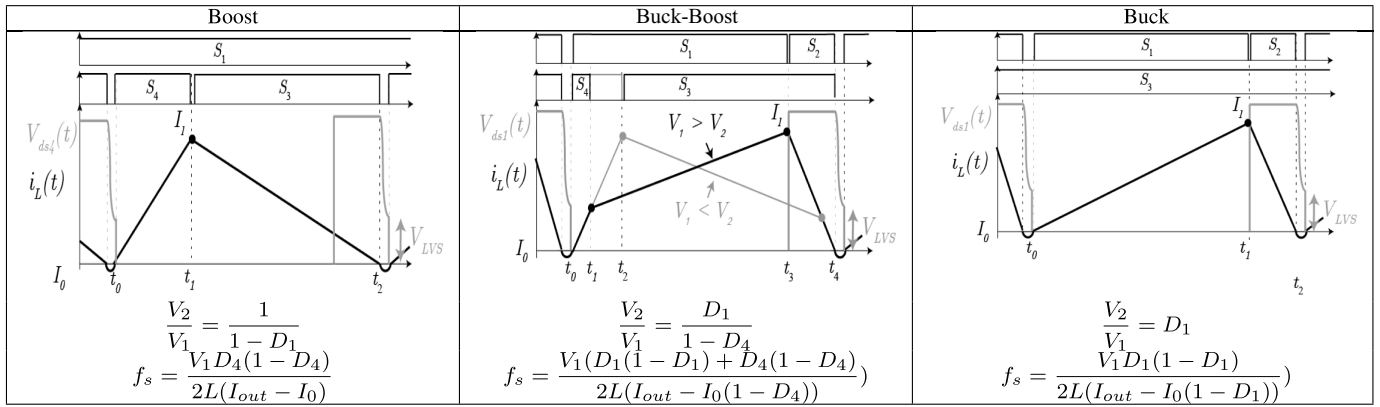
Note : Look-up table (LUT), Feed Forward (FF), Proportional (P), Integrator (I), derivator (D), Variable (V)/Constant (C) frequency (F), and Model Predictive Control (MPC).

minimize inductor RMS current [3], freewheeling current [6], and overall total losses [9], obtaining 98%, 98.3%, and 98.1% peak efficiencies, respectively. However, the resulting switching patterns are very complex and have three independent control variables, as shown under  $N_{ctrl}$  in Table I. As a result, complex 3-D look-up tables (LUTs) are required. Sufficient care has to be taken when designing these LUTs to prevent discontinuities and instabilities [5]. Additionally, for applications with wide voltage- and power ranges the LUTs can become very large and require external RAM/storage [1]. This complicates digital hardware design, and the data latency limits possible controller bandwidth. In [1] and [10], the authors overcame this by simplifying the switching pattern in order to reduce the size of the storage device and its data latency. Furthermore, in [8] Fang et al. further simplified the QCM switching pattern by defining a continuous and discontinuous QCM operating mode, with corresponding mode transitions, in order to completely negate the necessity of a LUT. The peak efficiencies obtained in [1], [8], and [10] are 98.5%, 99%, and 98.7% and thereby managed to simplify the control scheme while achieving slightly higher

peak efficiency. However, it should be noted that the reported efficiencies of studies focusing on QCM for sub-1-kW and sub-100-V converters do not, or not significantly, improve on the efficiency compared to much simpler continuous conduction mode (CCM) studies, such as [16] and [17], which report peak efficiencies of 98.5% and 99% in a similar power and voltage range.

For applications such as PV- or battery systems typically higher voltages are applied in the range of several hundreds of volt up to 1 kV, and as a result the effect of ZVS is much more significant. This is also observed in the high-peak efficiency reported in [2]. It should be noted that the peak efficiency of CF-QCM modulated FSBB converters is generally high for voltage gains close to one, but the efficiency tends to drop significantly when the gain starts to deviate from one. This is an inherent limitation of CF-QCM operation since higher input-output voltage differences increase the period  $T_x$  (see Fig. 2) which requires higher peak currents to compensate for the reduced power transfer [15]. This has been improved upon in [12], using a variable-frequency variation of QCM resulting in the highest reported efficiency for a QCM study, of 99.6%. Other variable-frequency modulations focus on triangular inductor current modulations, such as TCM and QR-BCM. In [13], Yu et al. use unipolar TCM in the buck and boost regions and bipolar TCM (B-TCM) in the buck-boost region. Despite the high-peak efficiencies of 99.5% in buck or boost mode, the high frequency and increased inductor root-mean-square (RMS) current in buck-boost mode significantly reduces the efficiency and form a bottleneck in the overall design. Additionally, the authors do not present a way to overcome the switching frequency discontinuity between the different operating modes. A recent study, presented in [15], has shown mathematically that three-mode TCM can achieve the highest possible efficiency of all full ZVS modulation strategies. However, this study (and all soft-switching modulations mentioned above) focuses on full ZVS and did not investigate QR-BCM or other ZCS possibilities and its analysis is therefore incomplete. Furthermore, no experimental comparison of the different modulation strategies is provided. Due to the emergence of wide bandgap semiconductors based on SiC and GaN, which already show significantly reduced switching losses, the tradeoff of increased peak or RMS current to achieve full ZVS

TABLE II  
SUMMARY OF BUCK, BUCK-BOOST AND BOOST OPERATION MODE



Note: For each operation mode the switching waveforms, voltage gain, and switching frequency are given. Please note that, for conciseness, the effect of the resonant period on switching frequency is not taken into account, as it has no impact on the power control discontinuity and only a small impact on the actual switching frequency as calculated in this table, and shown in Fig. 4.

should be reinvestigated and studies should not blindly focus on achieving full ZVS. To this extent, the literature related to QR-BCM, which has a lower increase in current and is simpler to implement, is lacking. Finally, none of the studies investigating VF TCM strategies have presented control schemes for closed-loop interleaved operation, nor presented a practical implementation to overcome the resulting power control discontinuities, which result from multimode operation.

To conclude, QCM is widely investigated but has inherent limitations, especially for wide voltage ranges. Furthermore, less studies have focused on triangular modulation schemes, despite reports of high efficiencies. Additionally, studies have provided theoretical proof that TCM can achieve higher efficiencies compared to QCM strategies, but experimental proof is missing and closed-loop control of multimode variable-frequency (MMVF) interleaved operation still needs to be investigated. Finally, most studies related to soft-switching are focusing on full ZVS, and more investigations into QR-BCM with wide bandgap devices is needed.

### A. Contribution

Based on the literature review presented above, the main contributions of this work are summarized as follows.

- 1) The first design of a 10 kW interleaved FSBB converter operating in closed-loop QR-BCM, including smooth mode transitions for MMVF operation.
- 2) A new control scheme is proposed that allows to simplify the switching pattern compared to QCM and TCM strategies and does not require any LUTs nor does it have an imperative requirement for high-frequency current measurement.
- 3) It is the first time that multiple soft-switching modulation schemes are experimentally compared and discussed. In this comparison, the proposed modulation showed the highest overall efficiency in an experimental comparison with three other soft-switching strategies (TCM,

bipolar (B-)QR-BCM, and QCM). With a peak efficiency of 99.6% the proposed control matches the highest efficiency measured in the literature [13], despite 67% higher power per phase. Especially, for wide-voltage-range applications, the efficiency can be significantly increased using the proposed modulation.

- 4) Our results show that adopting QR-BCM with zero-current switching (ZCS) allows simplifying the converter design and control, without a decrease in efficiency, compared to zero-voltage switching triangular current mode (TCM).

### B. Article Organization

The remainder of the article is organized as follows. Section II presents the proposed modulation. After which the design of the control loop is discussed in Section III, and the experimental verification is presented in Section IV. Next, the comparison with other soft-switching modulation strategies is done in Section V. Finally, the conclusion is presented in Section VI.

## II. MULTIMODE, VARIABLE FREQUENCY MODULATION

The switching waveforms for the proposed MMVF modulation strategy are shown in the figures in Table II. Additionally, the voltage gain ( $V_2/V_1$ ) and switching frequency  $f_s$  are calculated. Together these determine the on-time of the switches. For voltage gains significantly above or below 1, the converter operates as a variable-frequency synchronous boost or buck converter, with  $S_1$  or  $S_3$  always on, respectively. However, for voltage gains approaching unity, the switching frequency of both buck and boost mode approaches zero, as shown in Fig. 4. As a result, a power control discontinuity occurs. To overcome this, a third buck-boost mode is introduced. In this mode, both half-bridges are switching. As a result, compared to buck or boost mode, buck-boost mode has two additional degrees of

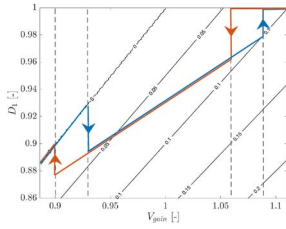


Fig. 3. Course of duty cycles  $D_1$  and  $D_4$  (surface), near the transition region, as calculated according to (1).

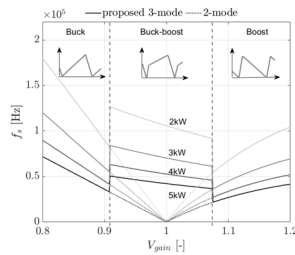


Fig. 4. Switching frequency when operating in QR-BCM: the proposed three-mode modulation versus two mode (buck or boost) operation. Without buck-boost mode, a power control discontinuity exists at  $V_{\text{gain}} = 1$ .

freedom: 1) the ratio of on-time for switches  $S_1$  and  $S_4$ ; and 2) their respective phase shift. It has been shown in [15] that minimizing the on-time of  $S_4$ , in combination with zero-phase shift results in the highest theoretical efficiency. Meaning that  $D_1$  should be maximized, and  $D_4$  minimized, for maximum efficiency. Therefore, to determine the ratio of  $(D_1/1 - D_4)$  for a given voltage gain, in buck-boost mode ( $V_2/V_1$ ), the maximum duty cycle of  $S_1$  is set to 98%, and minimum duty cycle for  $S_4$  is chosen to be 3%. After including 3% hysteresis in the transition region, the duty ratio in buck-boost mode can be determined by the linear curve drawn between the two outer limitations of the duty cycle ( $D_1^{\text{max}} = 0.98$  and  $D_4^{\text{min}} = 0.03$ ), as shown in Fig. 3. The resulting value of  $D_4$  can then be calculated according to

$$D_4 = D_4^{\text{min}} + \alpha \left( \frac{V_2}{V_1} - 0.9 \right) \quad (1)$$

Here,  $\alpha$  represents the linear slope that can be drawn between the two duty cycle extremes, as shown in Fig. 3. Next, the actual value of  $D_1$  is determined by the control output, resulting in the switching frequency for various output powers as shown in Fig. 4. As a result, the only remaining degree of freedom in the modulation is the selection of  $I_0$ .

#### A. Selection of $I_0$ : QR-BCM Versus TCM

From the switching waveforms and equations shown in Table III, it is clear that, besides the on-time of the switches, also the selection of the initial inductor current value  $I_0$  is a degree of freedom in the MMVF modulation. A value of  $I_0 = 0$  results in QR-BCM, which achieves ZCS with low-voltage valley switching ( $V_{VS}$  in Table II) or ZVS, depending on the in- and output voltage ratio. A value of  $I_0 = I_{ZVS}$  results in TCM, where  $I_{ZVS}$  is the necessary negative current offset to achieve full ZVS over

the entire voltage range. This negative current offset needs to be compensated by a higher peak current. Therefore, TCM results in a tradeoff between reducing switching losses and increasing conduction and core loss. Additionally, the negative current offset of TCM, and the higher peak-peak current, results in a slightly lower switching frequency for the same voltages and inductance. However, this effect is generally small as the current offset is in most cases significantly lower than the peak current. In the past, with silicon MOSFETs, full ZVS was often desired and was therefore likely investigated more. However, with the rise of wide bandgap semiconductors, the advantage of achieving full ZVS switching becomes less pronounced compared to their silicon predecessors. To analyze this, the differential equations given in Table III for the voltage over switch  $S_x$ ,  $v_{S_x}(t)$ , are solved algebraically for  $I_{ZVS}$  to achieve ZVS. For example, for boost mode the condition

$$v_{S_4}(I_0) = V_2 \quad (2)$$

is solved for  $I_0$  using the converter specifications, given in Table IV.

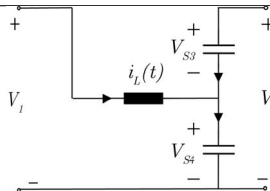
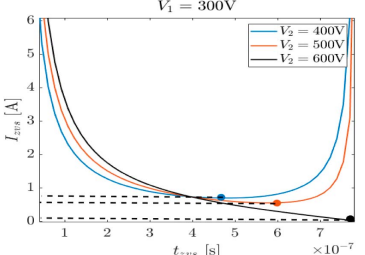
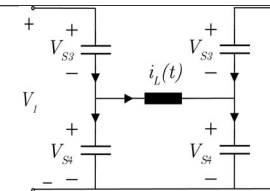
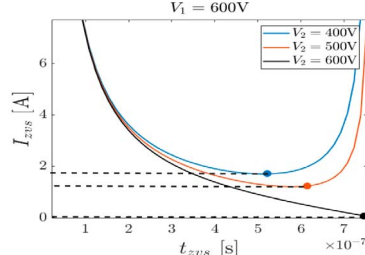
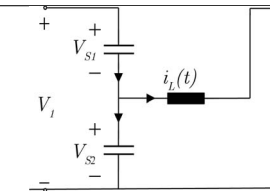
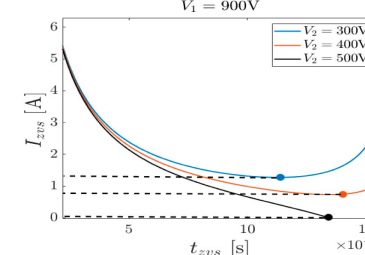
Using the resulting expression for  $I_0$ , the minimum value required to achieve ZVS:  $I_0 = I_{ZVS}$  and its corresponding dead time  $t_{ZVS}$ , can be determined and corresponds to the minimum of the  $I_{ZVS}$  curve shown in the figures in Table III.<sup>1</sup> In this analysis, the drain-source capacitances  $C_{ds}$  are averaged over the corresponding voltage range. Furthermore, the resonance capacitance  $C_r$  equals  $2C_{ds}$ , such that  $\omega_0 = (1/\sqrt{LC_r})$  and  $Z_0 = \sqrt{(L/C_r)}$ . Also, the minimum value of  $I_{ZVS}$  are used. The resulting values of  $I_0$  for all operating modes (with the largest possible voltage range for each mode) are shown in Fig. 5. It can be concluded as follow.

- 1) During buck operation, for any  $V_2 \geq (V_1/2)$ , ZVS turn-on of  $S_1$  can be achieved with  $I_0 = 0$ . Which holds for the majority of the specified voltage range in buck mode.
- 2) Similarly, in buck-boost mode  $S_1$  can turn-on with ZVS for  $V_2 \geq V_1$ . However, since this mode is only used for voltage gains close to one, the resulting switching losses for  $V_2 \leq V_1$  can still be significantly reduced as a result of valley switching with ZCS. Additionally,  $S_4$  can always turn-on with ZVS for  $I_0 = 0$ .
- 3) Finally, for boost operation  $V_2 \geq 2V_1$  needs to be met to achieve ZVS with  $I_0 = 0$ . As a result, in this operating mode TCM deviates the most from QR-BCM. The highest required value of  $I_0 = 3.43$  A, for  $V_1 = 850$  V and  $V_2 = 900$  V.
- 4) Finally, it is clear that, although the required value of  $I_0$  varies, ZVS can be achieved under QR-BCM in a significant part of the operation region. As a result, fixing  $I_0$  to the maximum required value over the whole range would result in suboptimal efficiency.

To calculate the tradeoff between capacitive switching losses for QR-BCM and the increased inductor current for TCM, all

<sup>1</sup>Please note that the combination of  $t_{ZVS}$ - $I_{ZVS}$  beyond the minimum  $I_{ZVS}$  corresponds to the second time that the condition  $v_{S_x}(I_0) = V_x$  is full filled in the resonance period. The first time that the condition is full filled corresponds to the value, before or at the minimum of  $I_{ZVS}$ .

TABLE III  
DIFFERENTIAL EQUATIONS FOR EACH OPERATING MODE DURING RESONANCE OF THE INDUCTOR WITH  
THE DRAIN-SOURCE CAPACITANCES OF THE CORRESPONDING FETS

Boost	Buck-Boost	Buck
 $i_L(t) = \frac{V_1 - V_2}{Z_0} \cos(\omega_0 t) - I_0 \sin(\omega_0 t)$ $v_{S4} = V_1 - (V_1 - V_2) \cos(\omega_0 t) - I_0 Z_0 \sin(\omega_0 t)$ $i_{zvs} = \frac{V_1 - (V_1 - V_2)(1 + \cos(\omega_0 t_{zvs}))}{Z_0 \sin(\omega_0 t_{zvs})}$ <p style="text-align: center;"><math>V_1 = 300\text{V}</math></p> 	 $i_L(t) = \frac{-V_2}{Z_0} \cos(\omega_0 t) - I_0 \sin(\omega_0 t)$ $v_{S1} = \frac{1}{2}(V_2(1 - \cos(\omega_0 t)) + I_0 Z_0 \sin(\omega_0 t))$ $v_{S4} = \frac{1}{2}(V_2(1 + \cos(\omega_0 t)) + I_0 Z_0 \sin(\omega_0 t))$ $i_{zvs} = \frac{2V_1 - V_2(1 - \cos(\omega_0 t_{zvs}))}{Z_0 \sin(\omega_0 t_{zvs})}$ <p style="text-align: center;"><math>V_1 = 600\text{V}</math></p> 	 $i_L(t) = \frac{-V_2}{Z_0} \cos(\omega_0 t) - I_0 \sin(\omega_0 t)$ $v_{S1} = \frac{1}{2}(V_2(1 - \cos(\omega_0 t)) + I_0 Z_0 \sin(\omega_0 t))$ $i_{zvs} = \frac{V_1 - V_2(1 - \cos(\omega_0 t_{zvs}))}{Z_0 \sin(\omega_0 t_{zvs})}$ <p style="text-align: center;"><math>V_1 = 900\text{V}</math></p> 

Note: Expression of  $I_{zvs}$  can be used to calculate the minimum amount of negative current offset required to achieve ZVS in that particular operating mode.

TABLE IV  
CONVERTER SPECIFICATIONS

$V_1$	$V_2$	$P/\text{phase}$	$N_{\text{phase}}$	Min-max $f_s$
300–900 V	300–900 V	5 kW	2	20–400 kHz

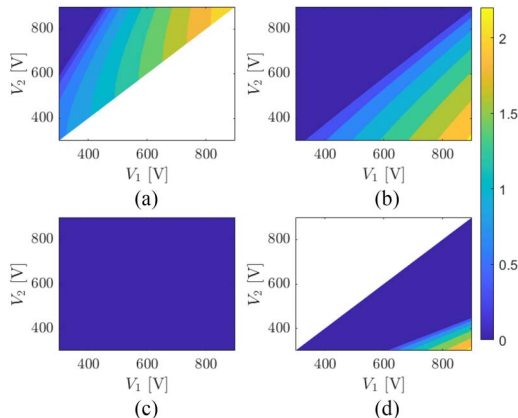


Fig. 5. Minimum value of  $I_0$  to achieve ZVS in (a) boost and (b) and (c) buck-boost ( $S_1$  and  $S_3$ ), and (d): buck mode respectively.

major losses in the converter need to be calculated. This is done according to

$$P_{\text{cond}} = \text{rms}(I_L)^2 R_{\text{on}}(T, I) + \text{rms}(I_{C_{1,2}})^2 R_{\text{ESR}}(f_s) \quad (3)$$

$$P_{\text{core}} = c_1 f_{\text{eq}}^{\alpha-1} \hat{B}^\beta f_s V \quad \text{with:} \quad (4)$$

$$f_{\text{eq}} = \frac{2}{\Delta B^2 \pi^2} \int_0^T \frac{dB^2}{dt} dt, \quad \text{and} \quad \hat{B} = \frac{\Delta B}{2} \quad (5)$$

$$P_{\text{switch}}^{\text{QR-BCM}} = \frac{1}{2} C_{\text{ds}} (V_{\text{VS}}) V_{\text{VS}}^2 + E_{\text{off}}(I, V, R_g) f_s \quad (6)$$

$$P_{\text{switch}}^{\text{TCM}} = E_{\text{off}}(I, V, R_g) f_s. \quad (7)$$

Here,  $\text{rms}(I_x)$  indicates the RMS current of  $x$ ,  $R_{\text{on}}(T, I)$  is the on-state resistance of the FETs extrapolated to current and temperature,  $R_{\text{ESR}}(f_s)$  the equivalent series resistance of the dc link capacitors, dependent on the switching frequency  $f_s$ ,  $B$  is the flux density in the inductor core, and  $V_{\text{VS}}$  indicates the valley-switching turn-on voltage under QR-BCM. The voltage dependency of the drain-source capacitance  $C_{\text{ds}}$  has been approximated based on power-law relationship, based on the datasheet. The resulting curve is then integrated, and averaged, to calculate the capacitive switching losses. Finally,  $E_{\text{off}}(V, I, R_g)$  are the turn-off losses which are scaled to the operating voltage, current, and gate resistance. Since boost operation shows the biggest deviation between QR-BCM and TCM occurs, it will be the focus of the remainder of this section. In this analysis, a 5-kW FSBB converter is assumed, based on UF3C120040K4S FETs and utilizing a 100  $\mu\text{H}$  inductor comprised of  $1000 \times 0.071$  mm litz wire and a 0077614A7 KoolMu core. The current dependency of the core is elaborated in the Appendix. From the results shown in Fig. 6, it is clear that aiming for full ZVS does not always result in the highest efficiency, as the higher peak-peak inductor current results in more conduction and core losses. Especially, when the value of  $I_0$  is fixed over the entire operating range, to simplify the control scheme. This results in significantly increased losses as

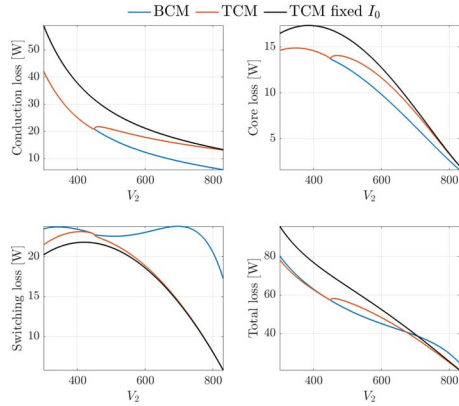


**Fig. 6.** Comparison of conduction losses  $P_{\text{cond}}$ , core losses  $P_{\text{core}}$ , switching losses  $P_{\text{switch}}$ , and total losses during boost operation with  $V_2 = 900$  V,  $P_1 = 5$  kW. The results are plotted for QR-BCM, TCM (with minimum  $I_0$ ), and TCM with a fixed value for  $I_0$  as is often implemented to simplify the control system.

it over estimates the required value of  $I_0$  in the entire operating region. Note that this calculation does not include the additional losses due to high-frequency current measurement using resistive shunts necessary for TCM. This high-frequency current measurement introduces additional complexity and losses, as discussed in the next section.

### B. High-Frequency Current Measurement

TCM operation requires a fast detection of a relatively small, but high frequency, negative current offset  $I_0 = -I_{\text{ZVS}}$ . This is usually done with low-resistive current shunts, which introduce additional losses. These shunts often have a resistance in the range of 20 m $\Omega$ . For the studied use case this would mean in an increase in conduction losses of 28.5%, resulting in a 10%–17% increase in total losses for TCM with minimum  $I_0$ , and a 17%–43% increase in total losses when the value of  $I_0$  is fixed over the entire operating range. These additional losses are often neglected in studies that only report open-loop measurements [13], [15]. Another option would be to use a very high-bandwidth current transducer. However, these are expensive and introduce delays, resulting also in increased losses. In contrast to TCM, QR-BCM does not have an intrinsic requirement for high-frequency current measurement, but can switch off with ZVS at a small positive current.<sup>2</sup> After that it uses the body diode of the FET, which automatically stops conducting at  $i_L = 0$ . This lowers the component count, reduces control complexity, and improves the efficiency.

Based on the analysis presented above, it is concluded that QR-BCM is the preferred modulation strategy for this FSBB converter, since the efficiency gain of TCM is marginal to none compared to QR-BCM and therefore does not justify the increased complexity. Especially when the inductor current needs

<sup>2</sup>When using QR-BCM the inductor current is never negative. As a result, it can be measured using current transformers. This is not the case for TCM since the current transformers cannot measure the dc-bias in the current, and therefore not detect when the inductor current is positive or negative.

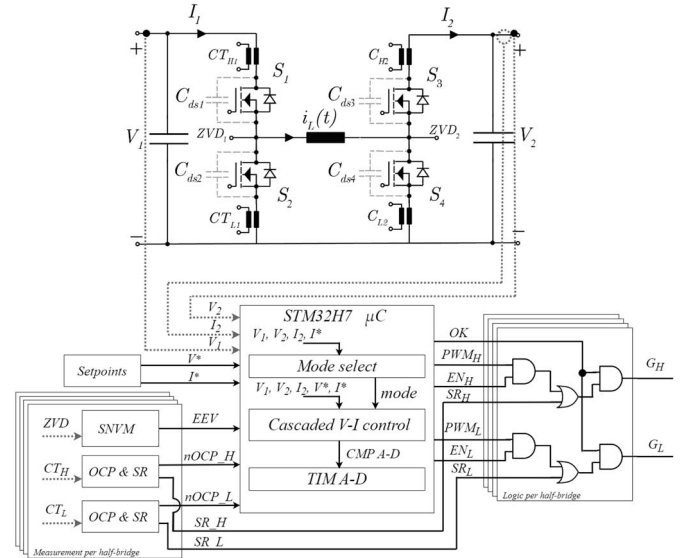


**Fig. 7.** Control diagram of the proposed three-mode QR-BCM scheme. The switch node voltage measurement (SNVM), over current protection (OCP), and synchronous rectification (SR) circuit are shown in more detail in Fig. 8.

to be measured by current shunts, or when it is fixed over the operating region.

Up to this point we have assumed three distinct modes of operation. In reality, the converter needs to be able to traverse these operating modes without a loss of output power. This requires a mode transition technique which is able to deal with the power control discontinuity resulting from the discontinuous step in switching frequency in between operating modes, as shown in Fig. 4. The implementation of this multimode interleaved QR-BCM control is discussed in the next section.

## III. MULTIMODE INTERLEAVED QR-BCM IMPLEMENTATION

The switching frequency discontinuity, shown in Fig. 4, causes a discontinuity in power control and can as a result cause extreme output power ripples, and trip the over-current protection. This section discusses the measures implemented to provide smooth and fast mode transitions. To do this, first, the general implementation of the digital control for interleaved QR-BCM is discussed, after which the mode transitions are explained.

### A. Digital Control for Interleaved QR-BCM

The control diagram of the proposed FSBB converter is shown in Fig. 7. It utilizes two interleaved phases to increase the power density by ripple cancellation. The fundamental waveforms for the converter in buck and buck-boost mode are shown in Fig. 9. The on-times of the first and second phase are identical, but the timers  $TIM C, D$  are shifted by 180 $^\circ$  with respect  $TIM A, B$  to ensure interleaving. This phase shift is measured using the master timer (MTIM) and updated every switching period. The first phase is always the master phase, and its timing measurements are copied to the second phase. Next, in buck



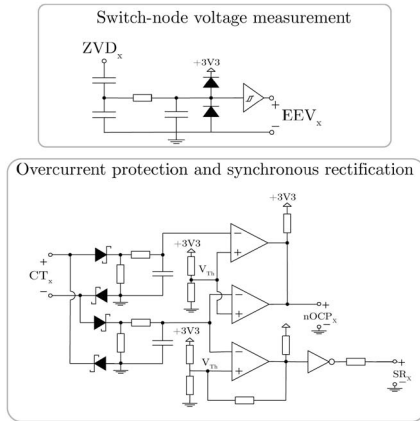


Fig. 8. Control circuitry for drain-source voltage valley detection, synchronous rectification, and overcurrent protection.

mode,  $S_3$  is always on; whereas, in boost mode,  $S_1$  is always on. The on-time of the active switch ( $S_1$  in buck and buck-boost mode and  $S_4$  in boost mode) is determined by the controller for a certain setpoint and corresponds to the comparator values  $CMP A$  and  $CMP B$ , respectively in Fig. 9. In case of buck-boost mode, the on-time of  $S_4$  is determined based on the on-time of  $S_1$  and the measured and low-pass filtered voltages  $V_1$  and  $V_2$ , according to (1). After the active switch has turned-off, the inductor current starts to decrease. In this case, the synchronous switch (complementary to the master switch) is on, until the inductor current falls below the threshold  $I_{Th}$ . This threshold is measured using current transformers on the drain and source of the top and bottom FETs, respectively as shown in Fig. 7. The current measurement circuit for synchronous rectification and overcurrent protection is shown in Fig. 8. Thanks to the logic circuitry shown in Fig. 7 the synchronous FET is turned-off despite the fact that the synchronous PWM signal ( $CH A_L$ ) is still high. Please note that synchronous rectification is optional, and the modulation itself has no high-frequency current measurement requirement. After the synchronous switch stops conducting, its body diode starts conducting until  $I_L = 0$ . Once  $I_L$  has dropped to zero, the LC resonance automatically occurs.

The resulting resonant voltage is measured at the switch node voltage ( $ZVD_x$  in Fig. 7) using the capacitive divider circuit shown in Fig. 8. By delaying the measured resonant voltage flank of  $ZVD_x$ , with an RC delay tuned to half the resonance period,<sup>3</sup> an external event  $EEV_x$  is created with a rising or falling edge (depending on the operating mode) at the time when the resonant voltage is minimal, or zero. The resulting rising- or falling-edge of the  $EEV_x$  then triggers a reset of the master switch PWM timer ( $TIMx$ ) and the  $MTIM$ . As a result, a new cycle is started when the drain-source voltage is at its minimum. Please note, that in case of full ZVS turn-on, the body diode of the switch already starts conducting ensuring ZVS

<sup>3</sup>The resonant period can be assumed fixed by placing a 470pF capacitance in parallel to the FET. Additionally, the parasitic  $C_{ds}$  flattens out above the minimum voltage of 300 V, and hence the total parallel capacitance can be considered constant.

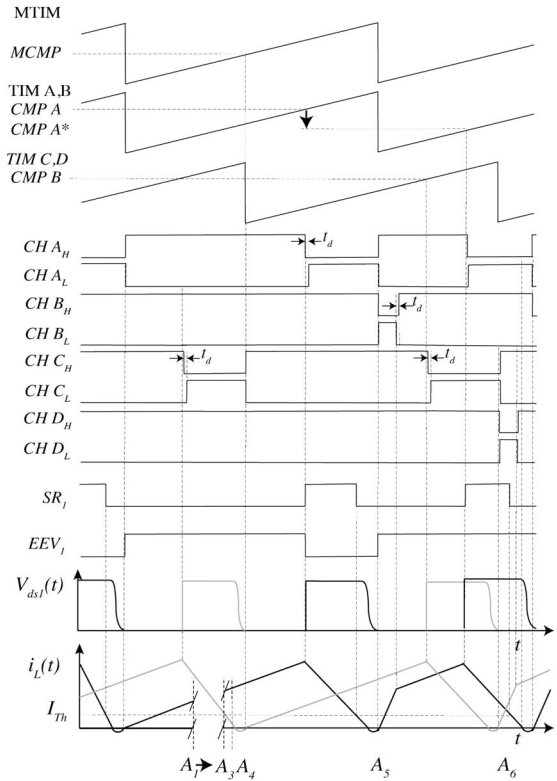


Fig. 9. Key waveforms for a two-phase interleaved FSBBC in buck mode. CH A,B correspond to the first phase and CH C,D to the second phase. The actions A1–A6 represent the timings of the mode transitions.

despite the fact that the switch has not turned on yet. In case of valley switching with ZCS, the switch is turned at  $(T_{res}/2)$ , which corresponds to the minimum drain-source voltage. The same  $EEV_x$  is also used to accurately measure the switching frequency and triggers an update of the registers that determine the phase shifts between the interleaved phases. As a result, the phase shift is updated every switching period, independent of the control loop frequency, and perfect interleaving is ensured. Finally, all PWM registers operate in preload mode and therefore are only updated when the accompanied timers are reset at every  $EEV$ . This allows the control loop to run at a fixed 25 kHz rate, and decouple it from the PWM frequency. Now that the basics of the QR-BCM implementation are discussed, the feed-forward mode transition technique can be explained in the next section.

## B. Feed-Forward Mode Transitions

To operate continuously in the entire operating region, mode transition mechanisms have been implemented. To prevent overshoots, each phase requires its own mode transition timing and needs to be executed when the inductor current of that phase equals zero. This is achieved using interrupt request (IRQ) handlers triggered by the corresponding  $EEV$  of that particular phase, after the voltage thresholds of the operating mode are exceeded. First, the master phase will transition, after which the IRQ of the second phase is enabled so that the same process order is always ensured. Depending on the required operating

mode, every transition is slightly different. However, the general procedure consisting of actions A1 to A6 is the same and is discussed in this section. An exemplary buck to buck-boost transition is shown in Fig. 9.

A1: At some point the voltage threshold of the existing operating mode is exceeded, once the duty cycle limitations of Fig. 3 have been reached. This initiates the transition procedure.

A2: Based on a given setpoint  $I_{set}$ , the switching period and on-times of the first cycles in the next operating mode are calculated. The on-times for each mode can be calculated according to (8)–(10).

For boost operation

$$T_{S_4} = \frac{2LI_{set}}{D_4V_1(D_4 - 1)}. \quad (8)$$

For buck-boost operation

$$T_{S_1} = \frac{2LP}{V_1(D_1^2V_1 - D_1^2V_2 - D_4V_2 + 2D_1D_4V_2)} \quad (9)$$

and for buck operation

$$T_{S_1} = \frac{4LI_{set}}{D_1(V_1 - V_2)}. \quad (10)$$

A3: The controller output, gain, and its internal variables are fed forward based on the calculations of action A2. Actions A1–A3 might take several switching periods depending on the switching frequency, as indicated by the broken x-axis in Fig. 7. In this time, a control update might be due. Therefore, a control update exception is activated to prevent register updates based on outdated information.

A4: After A1–A3, the mode transition is fully initialized, therefore any previous IRQ flags are cleared and the IRQ of the master phase is enabled. By enabling the IRQ handler, the mode transition will be executed at the next EEV.

A5: At the next EEV, the IRQ handler is executed. Inside the IRQ handler the following actions are taken.

- 1) The IRQ handler is disabled, preventing future EEVs from triggering an interrupt.
- 2) The corresponding PWM channel of the new master switch is activated.
- 3) The preload registers of the PWM timers and phase-shift are updated based on the calculated values ( $T_{S_1}$  or  $T_{S_4}$  above).
- 4) Next, the PWM timers (TIM A-D), phase shift controller (MCMP), the EEV, and the EEV sensitivity are reconfigured for the next operating mode.
- 5) The corresponding timers are reset, which updates the PWM timer registers based on the preload registers. Additionally, the set/reset configuration of the timers are updated corresponding to the new operating mode.
- 6) Finally, the second phase IRQ is enabled. By nesting the IRQ handler, it is ensured that the master phase IRQ is executed first. The phase 1 mode transition is now complete, and the phase starts operating in the new operating mode.

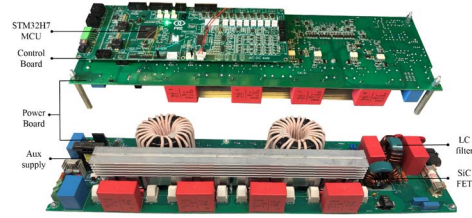


Fig. 10. Top and bottom side of the 10 kW interleaved cascaded buck-boost converter.

TABLE V  
PROTOTYPE SPECIFICATIONS COMPARED TO EXISTING STUDIES

Parameter	Proposed	[12]	[13]
$V_1$	300–900 V	300–500 V	400 V
$V_2$	300–900 V	200–600 V	100–500 V
Maximum power	10 kW	3 kW	3 kW
$\eta_{pk}$ @ max P	99.5%	99.5%	99.5%

A6: The EEV of the second phase initiates the transition of the second phase, following a similar procedure as the master phase (A5).

#### IV. EXPERIMENTAL RESULTS

The proposed modulation and closed-loop control scheme are implemented on an interleaved converter with 5 kW per phase (10 kW total), as shown in Fig. 10. The specifications are given in Tables IV and V. Furthermore, Fig. 11(a)–11(c) shows the three different operating modes, switching with full ZVS (under the measured conditions, full ZVS can be achieved with QR-BCM). Additionally, two example closed-loop mode-transitions at 10 kW are shown in Fig. 11(d)–11(e). Finally, Fig. 11(f) shows how the control can maintain a constant output current while traversing all three operating modes under a 200 V voltage step. The results demonstrate how each phase can transition smoothly and separately, at its own inductor current zero crossing, with a discontinuous step in switching frequency while preserving output power. By triggering the transition using the EEV, large current spikes are prevented, and each interleaved phase can transition at its own timing. Note that the current amplitude in buck-boost mode is lower for the same output power due to the trapezoidal current shape.

Next, all efficiencies are measured with a Yokogawa WT500 power analyzer with 0.1% specified power accuracy. The achieved efficiency is shown in Fig. 13. The efficiencies are measured with an output voltage  $V_2$  of 600 V, with  $V_1$  varying over the entire voltage region. The measured peak efficiency of 99.5% at full power and 99.6% at partial load occurs in buck operation with  $V_2 = 700$ . The buck-boost region shows the lowest efficiency due to the higher switching frequency and RMS currents. This confirms the assumption in Section II that the on-time of  $S_4$  should be minimized to maximize efficiency. The measured peak efficiency of the prototype matches the highest peak efficiency in the literature for the FSBB [12], [13], despite significantly larger power per phase and input voltage range, as shown in Table V. Additionally, these studies did

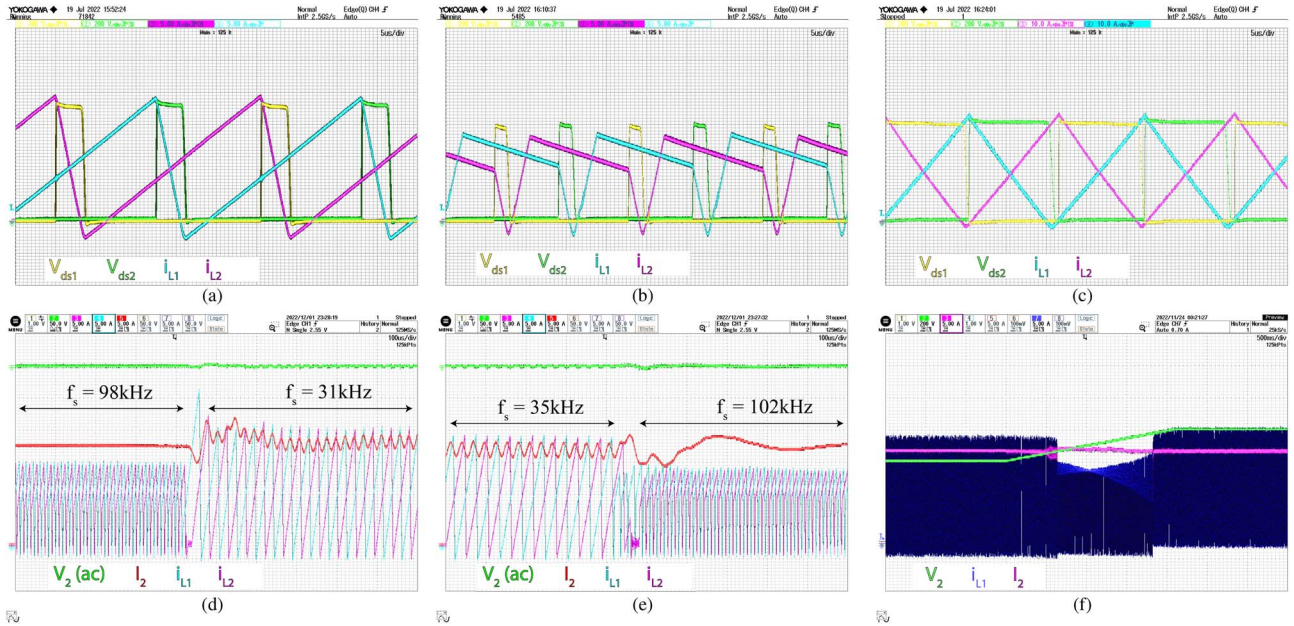


**Fig. 11.** (a)–(c) Inductor currents and drain-source voltages at 10 kW,  $V_o = 600$  V. (a) Buck  $V_i = 700$  V; (b) buck-boost  $V_i = 550$  V; and (c) boost  $V_i = 300$  V. (d)–(f) Closed-loop mode transitions at 10 kW  $V_o = 600$  V. (d) Buck-boost to buck mode; (e) boost to buck-boost; and (f) buck to buck-boost. Here,  $V_{ds,x}$  denotes the drain-source voltage of switch  $x$ , and  $I_{L,x}$  the inductor current of phase  $x$ , and  $V_2$  and  $I_2$  denote side 2 voltage and current, respectively.

not take into account the additional losses due to high-frequency measurement of  $I_0$ , as required for TCM. To further assess the performance of the proposed MMVF QR-BCM scheme, it will be compared with three other closed-loop FSBBC modulation schemes: TCM, and two other modulation schemes presented in [1] and [4].

### A. Experimental Comparison of Modulation Schemes

This section compares the proposed modulation scheme with three other soft-switching modulation schemes: TCM, B-QR-BCM, and QCM. All experimental comparisons are performed using the same 5-kW single-phase design, using the same prototype. Only the inductor will be redesigned to obtain the best results for each modulation scheme.

1) *Comparison With TCM:* To further examine the effectiveness of the proposed control a comparison based on efficiency, power density, and complexity is performed with three other soft-switching modulation schemes: QCM, B-QR-BCM and TCM. In the case of TCM, we have assumed  $I_0 = \min(I_{zvs})$ . In other words,  $I_0$  is the minimum required negative current offset to achieve ZVS. This is a significant assumption, as it requires additional control schemes to ensure this, therefore the value of  $I_0$  is often fixed to a larger value. Additionally, the TCM, QCM, and B-QR-BCM measurements are taken in open loop and do not factor in current measurement losses. To begin, Fig. 13 shows that the difference in efficiency between the proposed QR-BCM and TCM for  $300 \text{ V} \leq V_1 \leq 550 \text{ V}$  and  $V_2 = 600 \text{ V}$  is small. At full power, QR-BCM performs slightly better, whereas at partial power, TCM performs marginally better. This is a significant conclusion since most studies in the

literature always strive for full ZVS switching, even though the efficiency improvement compared to ZCS is none to negligible. Importantly, ZCS QR-BCM is significantly easier to implement since it does not require high-frequency current measurement or any ZVS tracking circuitry. The remainder of this section will be focused on the comparison with the QCM modulation presented in [4], and B-QR-BCM.

2) *Comparison With QCM and B-QR-BCM:* The modulation proposed in [4] provides a simplified QCM approach that allows to minimize the inductor RMS current while still having only one control variable. Second, B-QR-BCM is implemented. The main advantage of B-QR-BCM is that it only requires one operating mode for any voltage gain. All modulation schemes in this comparison can operate continuously over the entire voltage range and are controlled by a single control variable and therefore do not require LUTs of any sort. The simplified switching patterns are shown in Fig. 2, and the experimental waveforms under identical conditions are shown in Fig. 12(a)–12(c). The same single-phase prototype is used for all three schemes, apart from the inductor, which is optimized for every scheme. The inductance values and components used for each scheme are given in Table VI. For B-QR-BCM, higher permeability cores were used to achieve the higher inductance value.

3) *Efficiency:* The achieved efficiencies for full power and 50% partial power are shown in Fig. 13, and the calculated losses are shown in Fig. 12(d)–12(f). The calculations are done according to (3)–(6). Overall, the proposed modulation shows the highest efficiency for most voltage gains. This is achieved due to the low-RMS current combined with significantly lower switching frequency (at maximum power), as shown in

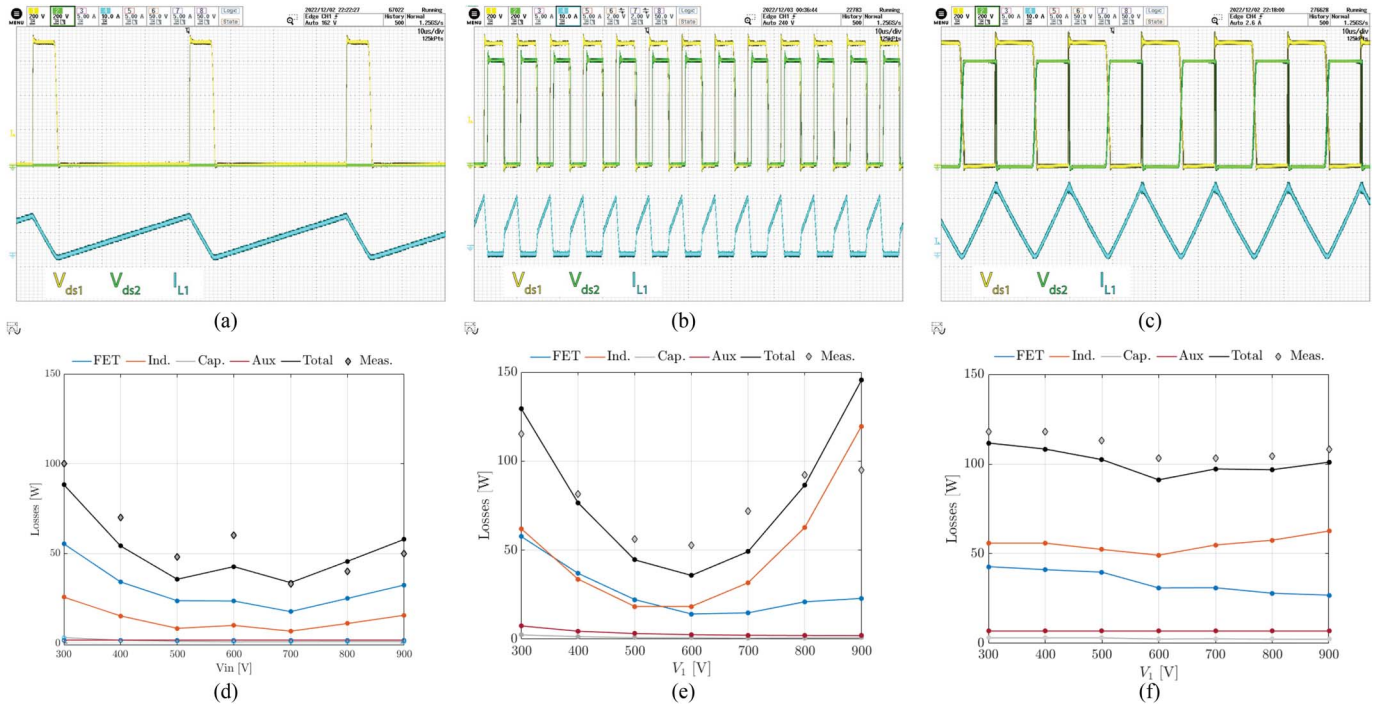


Fig. 12. (a) Proposed modulation (buck mode); (b) QCM modulation; (c) B-QR-BCM modulation, all measured at 50% partial load with 700 V input voltage and 600 V output voltage. (d)–(f) Loss distribution based on measured quantities at full power of 5 kW.

TABLE VI

COMPONENTS USED FOR THE CONVERTER DESIGN AND COMPARISON

	Proposed	B-QR-BCM	QCM
Inductance	100 $\mu$ H	275 $\mu$ H	35 $\mu$ H
Core	0077614A7	0077615A7	0077614A7
Litz wire	1000 x 0.071	1000 x 0.071	1000 x 0.071
FET	UF3C120040K4S	UF3C120040K4S	UF3C120040K4S
Capacitor	WIMA MKP-4	WIMA MKP-4	WIMA MKP-4

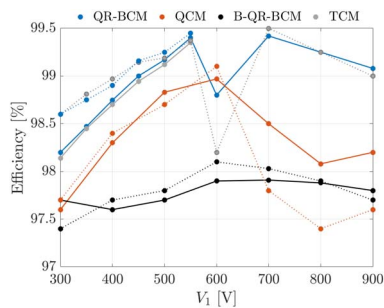


Fig. 13. Efficiency comparison of QR-BCM, QCM, B-QR-BCM, and TCM for  $V_2 = 600$  V at 2.5 kW (dotted) and 5 kW (line). The TCM measurements were measured in open-loop and therefore do not include losses due to current shunts. The results show there is no clear efficiency gain for using TCM compared to QR-BCM. At full power QR-BCM even out performs TCM. As a result, the added complexity required for TCM is unjustified.

Fig. 14(a)–14(c). Only for voltage gains close to 1 the QCM modulation performs slightly better. The reason for this is twofold. First, the QCM modulation appears to be operating at its best for voltage gains close to one, since for  $V_{gain} = 1$ ,

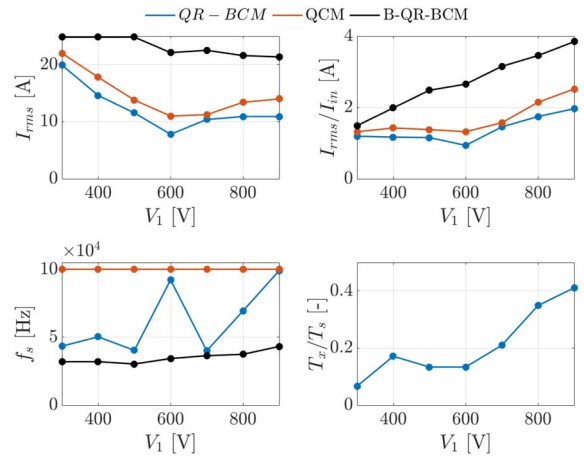


Fig. 14. Measured variation of the following variables for each modulation scheme: (a) RMS currents; (b) ratio of RMS- to input current; (c) switching frequency; and additionally, (d) shows the ratio of  $T_x/T_s$  with QCM. All were measured at 5-kW output power with varying input voltage.

$T_x = 0$ . As a result, almost the entire period is used for power transfer. Additionally, the buck-boost mode for QR-BCM operation is less efficient due to the trapezoidal current shape, resulting in higher frequency and RMS current than buck- or boost operation. The effect of  $T_x$  on QCM efficiency is visible from Fig. 14(a)–14(d): for voltage gains diverging from one,  $T_x$  increases which results in higher peak- and RMS currents, especially at high voltages. Fig. 12(e) shows that the core losses are most affected by this, as the high-peak currents and high-switching frequency result in a very high-equivalent frequency

[ $f_{eq}$  in (4)]. Physically, this is due to high-magnetizing losses resulting from high ( $dB/dt$ ) in the magnetic core. The effect on conduction losses is less significant due to the short duration of the peak currents. This is an inherent limitation of the constant-frequency behavior of QCM (note that lowering  $f_s$  does not solve this, as it would again increase  $T_x$ ). Another “disadvantage” of the QCM modulation scheme is the negative current offset  $I_{zvs}$  to achieve full ZVS, which as shown above does not necessarily outweigh the capacitive switching losses under ZCS, when wide bandgap FETs are used.

Regarding B-QR-BCM, its efficiency is compromised by a very high-inductor current which is inherent to the switching pattern of B-QR-BCM, where the inductor voltage is equal to the full in- and output voltage, when the  $S_1$  and  $S_4$  are on and off, respectively. For example, the peak inductor current in QR-BCM boost mode is twice the input current, i.e.,  $\max(I_L) = 2I_1$ . However, using B-QR-BCM the peak inductor current is equal to  $\max(I_L) = 2I_1/D_1$ . In other words, the full input power needs to be delivered in a relatively shorter part of the switching period, resulting in higher peak currents and resulting RMS currents. This naturally results in increased losses, especially due to the already higher inductance required.

## V. CONCLUSION

This article presented a closed-loop QR-BCM control scheme for the FSBBC, which addresses the problem of power control discontinuity under MMVF operation. The proposed control is applicable for both single- and multiphase converters. A two-phase 10 kW experimental prototype has been developed. Our experiments have shown that it is possible to provide almost instantaneous transitions between operating modes, without loss of output power. Additionally, with 99.5% peak efficiency, the measured efficiency equals the highest in the literature, despite a larger power- and voltage-operating range and based on a significantly simpler modulation scheme. This, in turn, is made possible by the ability to transition between different operating modes and optimize the modulation based on the voltage gain. Finally, a comparison with TCM, QCM, and B-QR-BCM has been performed. It is concluded that the proposed modulation scheme shows the highest overall efficiency, especially for wide-voltage-range applications, with limited- to no compromise in power density and complexity.

## APPENDIX

The used 0077614A7 core is a powder iron core which has a current dependent permeance. More specifically, the permeance reduces as the dc bias of the current increases. This can be modeled using

$$V_L(t) = L(t) \frac{di_L(t)}{dt} = (L_0 - K i_L(t)) \frac{di_L(t)}{dt} \quad (11)$$

Where  $L(t)$  is the time-varying inductance with  $L_0$  the inductance at zero current, which decrease with the slope  $K$ , and finally  $v_L$  and  $i_L$  are the inductor voltage and current. The

differential equation described above, can be solved for  $i_L(t)$  to obtain the expression described as follows [18]:

$$i_L(t) = \frac{L_0}{K} - \sqrt{\frac{L_0^2}{K^2} - \frac{2}{K} (V_L t + L_0 i_L(0) - \frac{K i_L(0)^2}{2})}. \quad (12)$$

The precise on-time for the converter can be calculated using (12). However, in the proposed converter two parallel 0077614A7 cores are used with a winding count 35 to obtain an inductance 100  $\mu$ H. As a result, the inductance reduction is not significant. Based on the specified permeance rolloff  $K$ , the permeance has reduced by only 7.5% at the maximum peak inductor current of 33 A. As a result, the switching frequency can be approximated using a fixed inductance value as shown in Table II, and its effect on controller design is negligible.

## ACKNOWLEDGMENT

The authors would like to thank Mike van den Heuvel and Joshua Jones from Power Research Electronics B.V. for their contribution to the developed prototype. This work is part of the FLEXgrid project.

## REFERENCES

- [1] L. Tian, X. Wu, C. Jiang, and J. Yang, “A simplified real-time digital control scheme for ZVS four-switch buck-boost with low inductor current,” *IEEE Trans. Ind. Electron.*, vol. 69, no. 8, pp. 7920–7929, Aug. 2022.
- [2] Z. Yu, H. Kapels, and K. F. Hoffmann, “Extreme high efficiency non-inverting buck-boost converter for energy storage systems,” in *Proc. PCIM Europe Int. Exhib. Conf. Power Electron., Intell. Motion, Renewable Energy Energy Manage.*, 2016, pp. 1–8.
- [3] Z. Zhou, H. Li, and X. Wu, “A constant frequency ZVS control system for the four-switch buck-boost DC-DC converter with reduced inductor current,” *IEEE Trans. Power Electron.*, vol. 34, no. 7, pp. 5996–6003, Jul. 2019.
- [4] K. Xia, Z. Li, Y. Qin, Y. Yuan, and Q. Yuan, “Minimising peak current in boundary conduction mode for the four-switch buck-boost DC/DC converter with soft switching,” *IET Power Electron.*, vol. 12, no. 4, pp. 944–954, 2019, doi: 10.1049/iet-pe.2018.5689.
- [5] S. Waffler and J. W. Kolar, “A novel low-frequency modulation strategy for high-power bidirectional buck + boost converters,” *IEEE Trans. Power Electron.*, vol. 24, no. 6, pp. 1589–1599, Jun. 2009.
- [6] Q. Liu, Q. Qian, B. Ren, S. Xu, W. Sun, and H. Li, “A new modulation strategy for four-switch buck-boost converter with reduced freewheeling current,” in *Proc. IEEE Appl. Power Electron. Conf. Expo. (APEC)*, 2020, pp. 2104–2108.
- [7] J. Yu, M. Liu, D. Song, J. Yang, and M. Su, “A soft-switching control for cascaded buck-boost converters without zero-crossing detection,” *IEEE Access*, vol. 7, pp. 32522–32536, 2019.
- [8] J. Fang, X. Ruan, X. Huang, R. Dong, X. Wu, and J. Lan, “A PWM plus phase-shift control for four-switch buck-boost converter to achieve ZVS in full input voltage and load range,” *IEEE Trans. Ind. Electron.*, vol. 69, no. 12, pp. 12698–12709, Dec. 2022.
- [9] Q. Liu, Q. Qian, M. Zheng, S. Xu, W. Sun, and T. Wang, “An improved quadrangle control method for four-switch buck-boost converter with reduced loss and decoupling strategy,” *IEEE Trans. Power Electron.*, vol. 36, no. 9, pp. 10827–10841, Sep. 2021.
- [10] F. Liu, J. Xu, Z. Chen, R. Huang, and X. Chen, “A constant frequency ZVS modulation scheme for four-switch buck-boost converter with wide input and output voltage ranges and reduced inductor current,” *IEEE Trans. Ind. Electron.*, vol. 70, no. 5, pp. 4931–4941, May 2023.
- [11] J. Liao, G. Qiu, Y. Huang, and V. Khadkikar, “Lagrange-multiplier-based control method to optimize efficiency for four-switch buck-boost converter over whole operating range,” *IEEE Trans. Ind. Electron.*, vol. 71, no. 1, pp. 822–833, Jan. 2024.

- [12] Z. Yu, H. Kapels, and K. F. Hoffmann, "A novel control concept for high-efficiency power conversion with the bidirectional non-inverting buck-boost converter," in *Proc. 18th Eur. Conf. Power Electron. Appl. (EPE'16 ECCE Europe)*, 2016, pp. 1–10.
- [13] Z. Yu, H. Kapels, and K. F. Hoffmann, "High efficiency bidirectional DC–DC converter with wide input and output voltage ranges for battery systems," in *Proc. PCIM Europe Int. Exhib. Conf. Power Electron., Intell. Motion, Renewable Energy Energy Manage.*, 2015, pp. 1–8.
- [14] G. Stahl, M. Rodriguez, and D. Maksimovic, "A high-efficiency bidirectional buck-boost DC–DC converter," in *Proc. 27th Annu. IEEE Appl. Power Electron. Conf. Expo. (APEC)*, 2012, pp. 1362–1367.
- [15] G. Yu, J. Dong, T. B. Soeiro, G. Zhu, Y. Yao, and P. Bauer, "Three-mode variable-frequency ZVS modulation for four-switch buck+boost converters with ultra-high efficiency," *IEEE Trans. Power Electron.*, vol. 38, no. 4, pp. 4805–4819, Apr. 2023.
- [16] L. Jia, X. Sun, Z. Zheng, X. Ma, and L. Dai, "Multimode smooth switching strategy for eliminating the operational dead zone in noninverting buck–boost converter," *IEEE Trans. Power Electron.*, vol. 35, no. 3, pp. 3106–3113, Mar. 2020.
- [17] N. Zhang, G. Zhang, and K. W. See, "Systematic derivation of dead-zone elimination strategies for the noninverting synchronous buck–boost converter," *IEEE Trans. Power Electron.*, vol. 33, no. 4, pp. 3497–3508, Apr. 2018.
- [18] G. R. Chandra Mouli, J. Schijffelen, P. Bauer, and M. Zeman, "Estimation of ripple and inductance roll off when using powdered iron core inductors," in *Proc. PCIM Europe Int. Exhib. Conf. Power Electron., Intell. Motion, Renewable Energy Energy Manage.*, 2016, pp. 1–8.



**Jos Schijffelen** received the bachelor's degree in electric engineering from Hoge Technische School, Leeuwarden, The Netherlands, in 1998.

In 1998, he started his career with Master-volt, Amsterdam, The Netherlands, and he was involved in design and manufacturing of Solar Inverters until 2002. In 2002, he took over the company Power Research Electronics BV (PRE) Breda, The Netherlands, together with Menno Kardolus.



**Gautham Ram Chandra Mouli** (Member, IEEE) received the bachelor's and master's degrees in electrical engineering from the National Institute of Technology Trichy, Trichy, India, in 2011, and the Delft University of Technology, Delft, The Netherlands, in 2013, respectively, and the Ph.D. degree in the development of a solar powered V2G electric vehicle charger from Delft University, in 2018.

He is an Assistant Professor with the DC Systems, Energy Conversion and Storage Group,

Department of Electrical Sustainable Energy, Delft University of Technology Delft, The Netherlands.



**Wiljan Vermeer** (Member, IEEE) received the master's and Ph.D. degrees in electrical engineering from Delft University of Technology, Delft, The Netherlands, in 2016 and 2023, respectively.

Currently, he is working with Fraunhofer-Institut für Zuverlässigkeit und Mikrointegration (IZM) Berlin, Germany, on high-power density converters based on embedded semiconductor power modules. His Ph.D. research interests include EV smart charging, battery degradation, and dc–dc power electronic converters for smart charging.



**Marck Wolleswinkel** received the bachelor's degree in electrical engineering from the Technical University, Delft, The Netherlands, in 2017.

Then, he started working as a Research & Development Engineer with Power Research Electronics with a focus on bidirectional EV chargers. He has worked on various new (bidirectional) power module concepts, both ac–dc (grid connected) converters and (isolated) dc–dc converters, with a special focus on digital control strategies and implementations on embedded

microcontrollers.



**Pavol Bauer** (Senior Member, IEEE) received the master's degree in electrical engineering from the Technical University of Kosice, Koišce, Slovakia, in 1985, and the Ph.D. degree in electrical engineering from Delft University of Technology, Delft, The Netherlands, in 1995.

He is currently a Full Professor with the Department of Electrical Sustainable Energy and the Head of the DC Systems, Energy Conversion and Storage Group, Delft University of Technology.